Tailoring negative pressure by crystal defects: Microcrack induced hydride formation in Al alloys

Ali Tehranchi [1,*] Poulami Chakraborty [1] Martí López Freixes [1] Eunan J. McEniry,[1] Baptiste Gault [1,2]
Tilmann Hickel [1,3] and Jörg Neugebauer [1]

[1]*Max-Planck-Institut für Eisenforschung GmbH, D-40237 Düsseldorf, Germany*
[2]*Department of Materials, Imperial College, South Kensington, London SW7 2AZ, United Kingdom*
[3]*BAM Federal Institute for Materials Research and Testing, D-12489 Berlin, Germany*

Climate change motivates the search for non-carbon-emitting energy generation and storage solutions. Metal hydrides show promising characteristics for this purpose. They can be further stabilized by tailoring the negative pressure of microstructural and structural defects. Using systematic *ab initio* and atomistic simulations, we demonstrate that an enhancement in the formation of hydrides at the negatively pressurized tip region of the microcrack is feasible by increasing the mechanical tensile load on the specimen. The theoretical predictions have been used to reassess and interpret atom probe tomography experiments for a high-strength 7XXX-aluminium alloy that show a substantial enhancement of hydrogen concentration at structural defects near a stress-corrosion crack tip. These results contain important implications for enhancing the capability of metals as H-storage materials.

I. INTRODUCTION

While fossil fuels have been a pillar of the rapid growth of modern human society, the ever growing consumption of coal, crude oil, natural gas, and their derivatives inflicts several challenges upon the human civilization [1]. Since the overall rise of global temperature [2] and climate changes are inevitable if the current rate of fossil fuel consumption is maintained, diversification of fuels is one of the most prominent responses to this crisis. The use of hydrogen as a non-carbon-emitting energy carrier is a very promising way of energy storage and carriage [3]. Metal hydrides (MH_x) are believed to be among the most technologically relevant classes of hydrogen storage materials because of their capability to be used in a diverse set of applications such as electrochemical cycling, thermal storage, heat pumps, and purification/separation [4]. The accumulation of H atoms is usually associated with an increase in the specific volume of the hydride phase. Thus, it can be envisioned that the presence of a *negative pressure* field will enhance the formation of these hydrides. Moreover, in contrast to ample studies on metal hydrides in the high (positive) pressure domain of phase diagrams [5], the negative pressure domain of phase diagrams remains largely unexplored due to experimental limitations (cf. [6–9]).

A possible way to overcome the experimental challenges is to carefully use crystal defects as laboratory tools to induce negative pressure at small scales. At this scale, the material can undergo stresses up to few GPa without loss of integrity. This negative pressure is present in close vicinity to edge dislocation or precipitates with larger atomic volume, such as Al_3Sc precipitates [10] in pure Al. However, in both cases, the magnitude of negative pressure cannot be adjusted externally.

Among the crystal defects, the stress field of preexisting and stationary microcracks not only depends on the material properties, but is also a function of the external loading. This is different from the stress fields of dislocations, precipitates, and grain boundaries, which are fully determined by the material and geometrical properties, but can hardly be changed during service. Thus one can tailor the magnitude of the negative pressure in the close neighborhood of this defect. On the one hand, it can thus be envisioned that the negative pressure domain of the phase diagrams can be explored. On the other hand, this mechanism might even give the chance to control the conditions of hydride formation and hydrogen release during discharging. This feature of microcracks improves the cyclability of hydride formation without requiring the formation of any new cracks in the material, i.e., a cyclic mechanical loading promotes charging/discharging cycles. However, finding the optimized crack density in the material that maximizes the hydride sizes and does not cause rupture is a major challenge. Nevertheless, there are a number of possible paths for controlling crack densities, such as exploiting intergranular cracks in nano-/micrograined materials or alloying.

In this work, we demonstrate, with *ab initio* and empirical potential based simulations, the theoretical feasibility of using microcracks as laboratory tools for inducing negative pressure and enhancing hydride formation. Based on the achieved
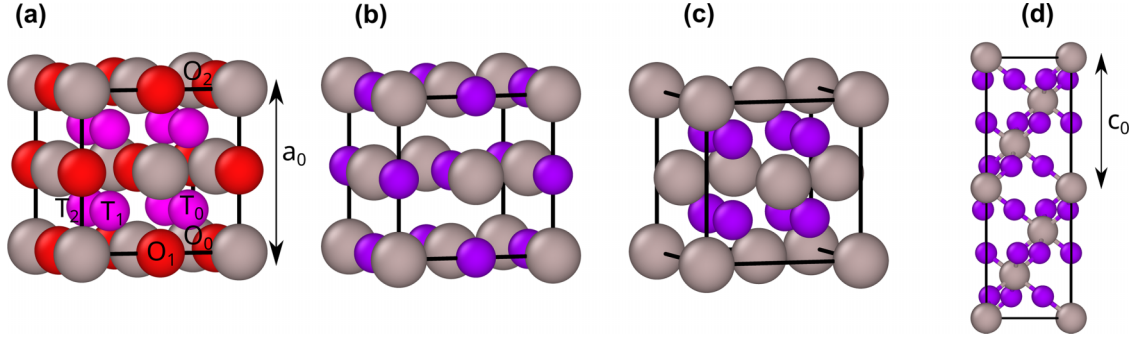
---

*tehranchi@mpie.de

FIG. 1. (a) Various tetrahedral (pink spheres) and octahedral (red) interstitial sites in Al (gray). The interaction energies between sites highlighted with the subscripts are given in Table I. Structure of (b) AlH, (c) AlH_2, and (d) Alane hydride, AlH_3. The gray and purple spheres denote Al and H atoms, respectively. The lattice constants of each structure are given in Table I.

theoretical insights, we reassess experimental evidence of the formation of high H concentration regions at crack tips using atom probe tomography (APT) and validate the theoretical predictions.

The study is prototypically performed for pure aluminum since it is a light (with $Z = 13$), cheap, and abundant element that seems to be a promising metal hydride former. Among the hydride phases in Al, the AlH_3, i.e., Alane hydride, is very efficient, having $\approx 11\%$ H gravimetric density, making this hydride "nearly perfect" for H-storage applications [11]. Al is not an intrinsically brittle material as compared to other light hydride-forming candidates such as Mg, and Li, making it even more attractive for hydrogen-storage solutions. For practical applications, the difficulty of recharging the hydride after H desorption can be addressed by loading/unloading the hydride simultaneously with the charging/discharging periods of the life cycle. However, the extremely high hydrogen gas pressures required for the hydrogenation of defect-free Al and the formation of metal hydrides at finite temperatures form one of the major challenges for the application of this hydride [11–13]. In this work, we suggest to meet this challenge by exploiting the concept of defect induced negative pressure. In this way, a route for designing metal hydrides is outlined, with potential impact for materials beyond the prototypical system in Fig. 1(a).

II. THERMODYNAMICS OF HYDRIDE FORMATION IN Al

A. Computational methodology of ab initio calculations

Density functional theory (DFT) calculations were carried out using the projector augmented wave (PAW) potentials as implemented in the Vienna *Ab initio* Simulation Package (VASP) [14–16]. The exchange and correlation terms were described by the generalized gradient approximation (GGA) proposed by Perdew, Burke, and Ernzerhof (PBE) [17]. A plane-wave cutoff of 500 eV was taken for all calculations. The convergence tolerance of the atomic force is 0.01 eV/Å and the total energy is 10^{-6} eV. Brillouin-zone integration was made using Methfessel-Paxton [18] smearing. Ionic relaxations were allowed in all calculations keeping the shape and volume fixed. The equilibrium structure of Al with a lattice parameter of 4.04 Å obtained within the convergence criteria is consistent with previous DFT-GGA calculations and has been used to construct the supercells.

B. Solubility of H in Al

The solution energy of an H atom in the Al matrix is determined using DFT, i.e., $E_{sol}^{tet} = E(Al_nH) - \mu_H^0 - E(Al_n)$. Here, $E(Al_nH)$ and $E(Al_n)$ are the energies of supercells with and without one H in an interstitial site in fcc Al_n, respectively. Since we are interested in H charging processes, which are

TABLE I. Selected properties of H in Al calculated by DFT, an angular-dependent potential (ADP) [24], and an augmented ADP in conjunction with a Morse potential (ADMP). $\Delta E_{sol}^{T \to O} = E_{sol}^O - E_{sol}^{tet}$ is the difference between the solution energy of H atoms in tetrahedral and octahedral sites. $E_{int}^{i,j,mNN}$ is the interaction energy of sites i and j in the mth nearest-neighbor configuration. The numbers in brackets denote the formation energy of pairs with respect to individual isolated H atoms in T sites. $E_f(AlH_m)$ is the formation energy per formula unit (f.u.) of the AlH_m phase at $\Delta\mu = 0$. ΔV denotes the excess volume of H atoms, and the hydrides in the Al matrix. The different sites are depicted in the figure. The interstitial sites and the structure of the hydrides are shown in Figs. 1(a)–1(d).

Quantity	DFT (this work)	ADP [24] (this work)	ADMP (this work)
$\Delta E_{sol}^{T \to O}$ (eV)	0.102	0.131	0.131
$E_{int}^{T_0, T_1, 1NN}$ (eV)	-0.114	0.007	-0.114
$E_{int}^{T_0, T_2, 2NN}$ (eV)	-0.028	-0.007	-0.031
$E_{int}^{O_0, O_1, 1NN}$ (eV)	$-0.111(0.093)$	0.002	-0.057
$E_{int}^{O_0, O_2, 2NN}$ (eV)	$-0.061(0.143)$	-0.016	-0.016
$E_{int}^{O_0, T_0, 1NN}$ (eV)	$-0.086(0.016)$	0.031	-0.080
$E_{int}^{O_0, T_1, 2NN}$ (eV)	$-0.086(0.016)$	-0.007	-0.027
$E_f(AlH)$ (eV/f.u.)	0.740	0.784	0.637
$E_f(AlH_2)$ (eV/f.u.)	0.895	1.179	0.269
$E_f(AlH_3)$ (eV/f.u.)	-0.152	1.125	0.093
ΔV (H) (Å^3)	1.808	2.720	2.720
ΔV (AlH) (Å^3)	-0.027	1.763	-0.149
ΔV (AlH$_2$) (Å^3)	3.585	2.861	1.646
ΔV (AlH$_3$) (Å^3)	17.652	15.657	11.852
a_0 (Al) (Å)	4.04	4.04	4.04
a_0 (AlH) (Å)	4.037	4.18	4.026
a_0 (AlH$_2$) (Å)	4.31	4.26	4.17
c_0 (AlH$_3$) (Å)	5.92	5.69	3.97
AlH bond length (AlH$_3$) (Å)	4.22	4.05	3.69

usually expressed in terms of the H_2 gas pressure, we consider the chemical potential of the H_2 molecule $\mu_H^0 = \frac{1}{2}E(H_2)$ as a reference. Note that this value does not contain any finite temperature and pressure contribution of the gas phase. Thus the chemical potential of H can become larger than this value at finite T and pressures [19]. We find the tetrahedral sites to be more favorable for H (solution energy of 0.743 eV) than octahedral sites (0.845 eV), in accordance with previous studies in the literature [20]. Further, we reveal significant first (-0.114 eV) and weaker second (-0.028 eV) nearest-neighbor attractive interactions between two H atoms in the tetrahedral sites of Al (cf. Table I). The application of a negative pressure of 4 GPa increases the first nearest-neighbor interaction by only $+0.012$ eV (see Sec. S1 in the Supplemental Material [21]), i.e., it has a small impact on the interaction energy. Attractive interaction energies that are larger than $k_B T$ at room temperature (≈ 0.03 eV) facilitate the population of H atoms in the defected regions. As previously shown for Ni [22], nanohydrides would not exist in defected regions without the existence of these interactions, even for the maximum relevant H bulk concentrations, C_b, in Al (≈ 1000 appm) [23]. Though attractive interactions are also determined for pairs containing octahedral sites, they cannot compensate for the energetic preference of the tetrahedral sites indicated above.

Due to the extensive computational costs, the large-scale atomistic simulations required for defects such as cracks are not possible using DFT. In this work, the interaction between atoms next to cracks is therefore described by an angular-dependent potential (ADP) [24]. The ADP has already been successfully used for the modeling of H-Al interactions [25,26] and allows us to efficiently model extended defects within supercells with $\approx 10^5$ atoms. For the original version of the ADP, the H-H interaction energies are significantly lower than those obtained via DFT (cf. Table I). To include these crucial features, we augmented the ADP by the addition of an attractive Morse-type interaction between H atoms, which we call ADMP (see Sec. S4 in the Supplemental Material [21]).

C. Formation energies and excess volumes of different hydride phases

1. Excess volumes of hydride phases

Our study of hydrides in Al is focused on the most stable candidates at each stoichiometry, i.e., the rock-salt type AlH, the flourite type AlH_2, and the α-Alane hydride AlH_3 [20]. To determine the influence of stress, the excess volume of the hydrides is important, which has been computed as the difference between the fully relaxed volume of the hydride supercell per Al atom, $V(Al_m H_n)/m$, and that of the metal, $V(Al) = 16.48$ Å^3, at zero pressure. The contribution of each H atom to this excess volume can be computed by further multiplying of excess volume by m/n. The excess volume will couple with the stress field through a $-p\Delta V$ term and will decrease the formation energy of hydrides in negatively pressurized regions of the material. The DFT-determined excess volume of AlH_3 is particularly large (≈ 18 Å^3) and thus its interaction with the tensile stress field of the cracks will be considerable (Table I). In the case of AlH_2, the excess volume remains positive, but its magnitude is ≈ 5 times smaller than
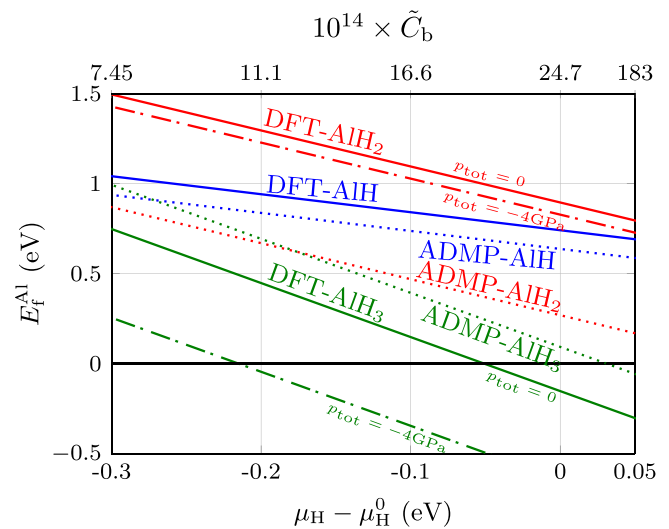

FIG. 2. Formation energy per formula unit (f.u.) of the different Al hydride phases vs the hydrogen chemical potential based on DFT and ADMP simulations. The solid, dashed, and dotted lines denote results for DFT at zero total pressure, DFT at negative total pressure, and ADMP at zero total pressure, respectively. Green, red, and blue lines denote AlH_3, AlH_2, and AlH, respectively. The upper horizontal axis denotes $\tilde{C}_b$, the atomic bulk concentration of H atoms at room temperature.

that of AlH_3. Interestingly, in the case of rock-salt AlH, the excess volume is very small but negative. We conclude that the effect of the stress fields on the hydride formations is only significant for AlH_3.

The ADMP follows the qualitative trend of the excess volumes of the hydride, however with less magnitude. We also calculated the excess volume of a single H atom in Al bulk ($\Delta V(H) = 1.808$ Å^3) by constructing the pressure-concentration plots and calculating the excess volume using their slope [27]. The excess volume of individual H atoms is important to trigger their long-range diffusion in the bulk towards the defected regions. The resulting increase of the H concentration in these regions makes the formation of hydrides possible.

A comparison of this excess volume with the excess volume per H atom in the unit formula in the hydrides indicates an increase by a factor of 3.25 in the case of AlH_3. For AlH_2 and AlH, this factor is 0.99 and -0.015, respectively. This observation also demonstrates the strong effect of a negative stress field as a driving force for the formation of covalently bonded trihydride AlH_3 out of H populated regions.

2. Formation energies of hydrides

The formation energy per atom $X \in \{Al, H\}$ of each phase is given by

$$E_f^X = \frac{1}{n_X}[E(Al_{n_{Al}} H_{n_H}) - n_{Al}E(Al) - n_H\mu_H], \quad (1)$$

where $E(Al_{n_{Al}} H_{n_H})$ is the energy of the supercell containing the hydride, and $E(Al)$ is the energy per atom in bulk fcc Al. In the case of bulk hydride phases, and planar defects, $X = Al$ and $X = H$ are, respectively, relevant. The DFT calculations yield the α-Alane hydride as the most stable phase at $\mu_H =$

μ_H^0 (Fig. 2, Table I). Moreover, the results indicate that the formation of AlH$_3$ becomes exothermic at chemical potentials $\mu_H - \mu_H^0 \geqslant -0.05$. The lacking observation of these hydrides at the low experimental H concentrations (≈ 1000 appm) is probably due to the fact that the crystal structure of AlH$_3$ is significantly different from fcc Al, resulting in high nucleation barriers for their formation [28]. The exothermic formation of AlH$_3$ is also present in the case of the ADMP since $E_f^{Al}(AlH_3)$ is closer to the DFT value after the modification of the ADP by the Morse potential. There are a number of discrepancies between ADMP and DFT, e.g., the overstabilization of the AlH$_2$ hydride, but they do not affect the trends for the hydride formation and the results of the upcoming molecular dynamics-Monte Carlo (MD-MC) simulations. The reason is that the DFT calculations depicted in Fig. 5 show that the AlH$_2$ hydride is also stable with respect to individual H atoms in the chemical potential domain in which the MD-MC simulation are performed and can serve as a nucleus for AlH$_3$. In other words, AlH$_2$ provides a chemical driving force for AlH$_3$ formation, which overcomes the structural differences hindering this process. In this regard, the simulation using ADMP provides a lower bound for the enhancement effect of the crack tip regions. Beyond the values at $\mu_H = \mu_H^0$, Fig. 2 depicts the formation energy of different Al hydrides versus a variation of the chemical potential μ_H for both pressure-free and negative pressure cases. In addition, the top axes in Fig. 2 show the bulk concentration of H atoms in the fcc bulk Al solid solution for the corresponding chemical potentials at $T = 300$ K using the relation

$$\tilde{C}_b = \rho_{tet} \exp\left[-\left(\mu_H^{tet} - \mu_H\right)/k_B T\right], \quad (2)$$

where $\rho_{tet} = 2$ is the ratio of tetrahedral sites to lattice sites of fcc Al and μ_H^{tet} is the energy for the insertion of H in a tetrahedral site of bulk Al, i.e., $\mu_H^{tet} = E_{sol}^{tet} + \mu_H^0$. It is evident that the most stable hydride is AlH$_3$. Another important observation is that the formation energy of AlH and AlH$_2$, for which the fcc lattice for Al atoms is maintained, is positive in the whole domain of chemical potentials. Given the large attractive H-H interactions in fcc Al (cf. Table I), the high formation energies for these two hydrides is attributed to the *repulsive many-body interaction* of H atoms within the hydride [29].

As explained above, the effect of pressure p is included in the model by adding the $-p\Delta V$ term. Throughout this work, we refer to the mechanical pressure induced by defects and external mechanical loadings as $p^{(m)}$, i.e., the total pressure acting on the hydride is $p_{tot} = p_{H_2} + p^{(m)}$. The approximation arising from discarding the other components of the stress field does not change the picture, as proven in Sec. S3 of the Supplemental Material [21] using the method of Sih *et al.* [30]. Note that in the case of the cracks, the stress field of external mechanical loading and the defect are coupled through the stress intensity factor, while in the case of some other defects such as dislocations, the two aforementioned stress fields are not directly coupled. It can be seen that the α-Alane hydride remains to be the most stable hydride for all relevant values of the chemical potential, in accordance with [20]. A negative pressure field of magnitude $p_{tot} = -4$ GPa significantly reduces the formation energy of α-Alane, whereas this effect is negligible for the other hydrides. The choice $p_{tot} =$

-4 GPa corresponds to the maximum pressure achievable in the close (a few Ångstroms) neighborhood of the crack tip before the emission of dislocation or decohesion [31]. Moreover, this pressure is well below the theoretical tensile strength of Al of $\sigma_{max} = 12$ GPa [32]. The results of the ADMP in Fig. 2 also yield AlH$_3$ as the most stable phase above $\Delta\mu = -0.175$ eV, but the AlH$_2$ phase is more stable than the AlH phase. However, we only use this potential for the simulated accumulation of individual H atoms at the crack tip region; moreover, the most stable hydride is conserved by the ADMP. Thus the overstabilization of AlH$_2$ and H clusters beyond pairs, due to the presence of strong H-H attractive interaction, is not affecting the results of our study. It also should be noted that the DFT calculations depicted in Fig. 5 also show that the AlH$_2$ hydride is more than lattice gas in the chemical potential regions in which the ADMP simulations will be performed.

3. Pressure-dependent phase diagram of Al-H

We next construct the phase diagram of the hydrides for different temperatures and chemical potentials. To this end, it is necessary to calculate the vibrational entropy contribution to the free energy of the formation of the hydride phases,

$$F_f(Al_m H_n) = E_f(Al_m H_n) + F^{vib}(Al_m H_n) - m F^{vib}(Al)$$
$$- \frac{n}{2} F(H_2). \quad (3)$$

Here, the vibrational free energy F^{vib} is calculated via the quasiharmonic approximation [33] (see Sec. S5 of the Supplemental Material [21]). The temperature-dependent part of the formation energy of the H$_2$ molecule is determined using the experimental relation [20]

$$F(H_2) = \frac{7}{2}k_B T - T S^{expt}(H_2), \quad (4)$$

where k_B is the Boltzmann constant, T is the temperature, and $S^{expt}(H_2) \approx 15.7 k_B$. The enthalpy and entropy of the H$_2$ molecule are evaluated at standard conditions, respectively [34]. The vibrational contributions to the free energy of Al and its hydrides are substantially smaller than the finite-temperature entropy of the H$_2$ gas (see Sec. S5 of the Supplemental Material [21]). This result is in accordance with the findings of Wolverton *et al.* [20]. Thus we neglected the effect of the stress field on the vibrational contribution of solid states.

Figure 3 is the pressure-dependent phase diagram of the hydrides in terms of different temperatures and hydrogen chemical potentials. Consistent with the $T = 0$ K results, the α-Alane hydride is stable for high μ_H values and the competing phase is pure Al accompanied by H$_2$ gas. The white solid lines denote the border of the two aforementioned phases at various p_{tot} values. It can be seen that negative pressure significantly enhances the formation of AlH$_3$ for given temperatures as well as for given chemical potentials, and no hydride AlH$_n$ with $n < 3$ becomes stable. The pressure dependence of the chemical potential of hydrogen can be expressed in terms of the external H$_2$ gas pressure p_{H_2} as

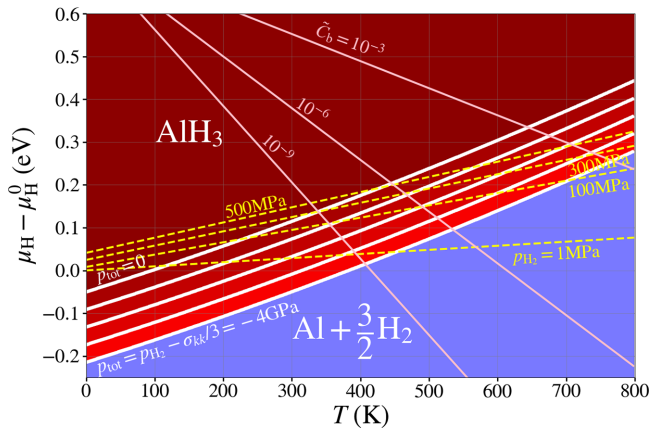$$\mu_H = \mu_H^0 + \frac{1}{2}\left[(p_{H_2} - p_0)b + k_B T \ln \frac{p_{H_2}}{p_0}\right], \quad (5)$$

FIG. 3. Pressure-dependent phase diagram of AlH$_3$ hydride in $\mu - T$ space. The dashed lines denote the variation of the chemical potential of H$_2$ gas for various p_{H_2} obtained using Eq. (5). The pink lines denote the isobulk concentration lines.

where $p_0 = 0.1$ MPa is the standard pressure [35]. The co-volume constant $b = 26.3$ Å^3 accounts for the volume of a H$_2$ molecule in the Nobel-Abel equation of state. Figure 6(a) illustrates the mechanical pressure-dependent phase diagram of the α-Alane hydride in $p_{H_2} - T$ space. It can be seen that the presence of a negative mechanical pressure field in the Al matrix significantly reduces the required p_{H_2} for the formation of the α-Alane hydride. This feature is the most important message of this work.

4. Long-living metastable planar defect in the Al-H system

After having established the pressure-dependent phase diagram of the Al-H system, we turn our attention to the planar defects observed in experiments. Interestingly, our experimental results indicate the presence of hydrides along (111) planes at the crack tip region. Hence, we computed the formation energy of several planar hydrides in fcc Al. Their atomistic configurations are given in Figs. 4(k)–4(l). Figure 5 depicts the formation energies per H atom of the most stable planar
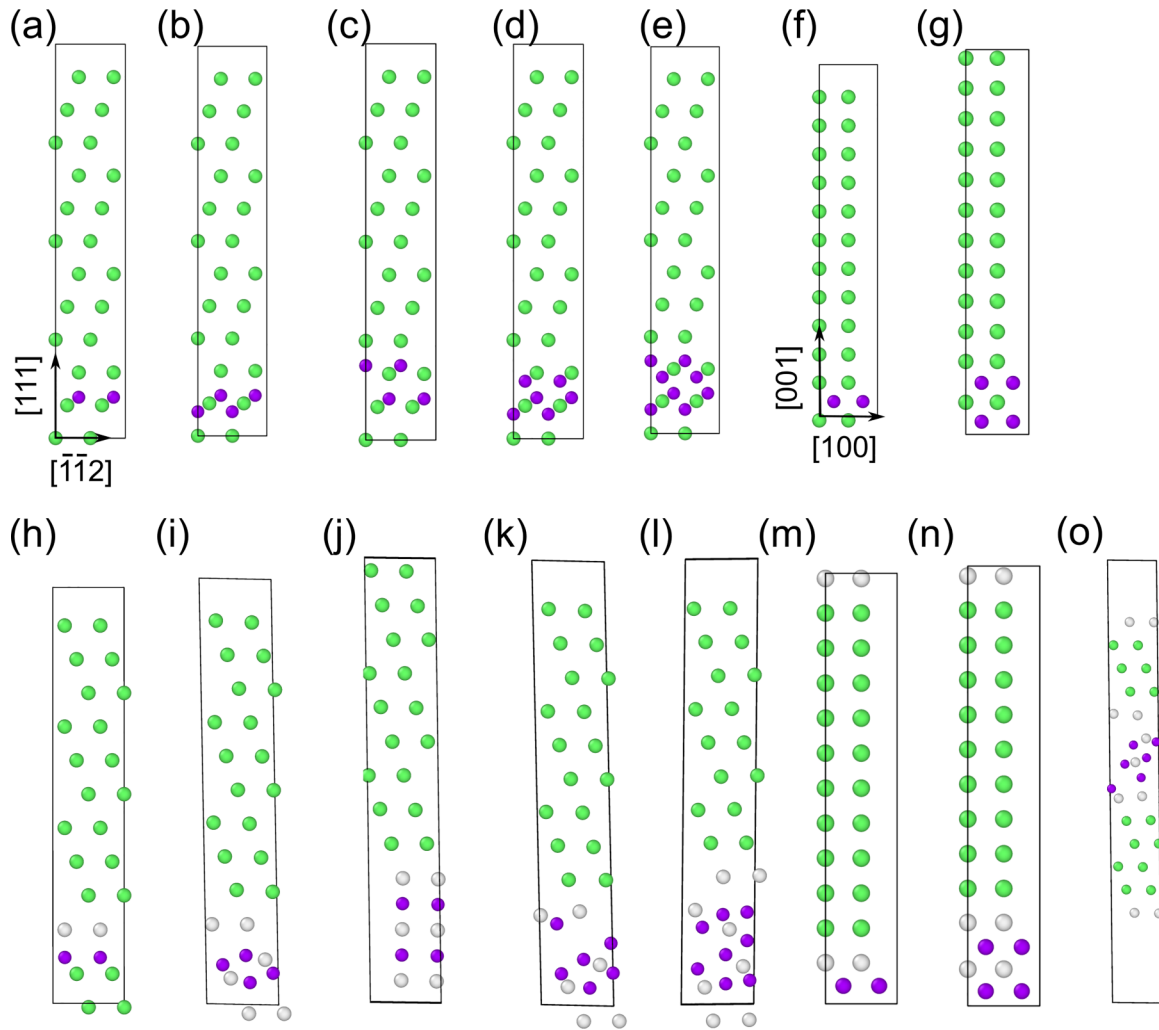
FIG. 4. Initial structure of the supercell containing (a) one layer of H along (111), (b) two neighboring layers of H along (111), (c) two layers of H along (111), (d) three neighboring layers of H along (111), (e) four neighboring layers of H along (111), (f) one layer of H along (100), and (g) two neighboring layers of H along (100) planes. (h)–(n) The final structures of the aforementioned planar hydrides with the same order. (o) The relaxed structure of the supercell containing a stacking fault in a three-layered hydride at the (111) plane. The green, white, and purple spheres denote the fcc-Al, unrecognized-Al, and H atoms, respectively.

FIG. 5. Formation energy per H atom of the different Al planar and bulk hydrides phases vs the H chemical potential based on DFT. The range of chemical potentials chosen here is relevant for the competition of the defect and bulk phases with the H atoms solved in the T site of fcc Al. 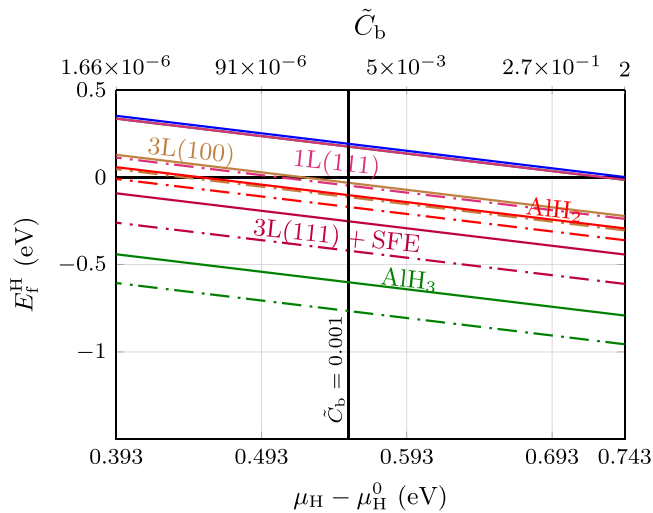The vertical black line denotes $\tilde{C}_b = 1000$ appm at $T = 300$ K, which is close to the bulk concentration in the experimental work of Birnbaum *et al.* [23]. The solid and dashed lines denote the results for DFT at zero pressure and negative pressure, respectively.

hydrides in addition to the bulk hydrides with respect to the chemical potential of a single H atom in the tetrahedral site in fcc Al, i.e., $\mu_H - \mu_H^0 = \mu_H^{tet} - \mu_H^0 = 0.743$ eV.

This situation corresponds to the formation of a hydride with all T sites occupied by noninteracting H atoms, which is clearly unfavorable with respect to AlH$_n$ hydrides. We particularly use the formation energy per *H atom* to compare the driving force of H atoms into these planar defects with their energy in the bulk hydride phases. It can be seen that the planar hydride consisting of three layers of H atoms along a (111) plane containing a stacking fault is the most stable structure in comparison to all hydrides except AlH$_3$. This observation corroborates the experimental observation of Birnbaum *et al.* [23] in which an enrichment of H atoms on platelets in {111} planes is reported. The application of negative pressure does not change this observation. The reason for the preference of the (111) plane is that H atoms along these planes can distort the Al matrix and find an energetically favorable structure that is similar to the AlH$_3$ structure, while these distortions are absent in AlH$_2$ and planar hydrides along (100) planes, i.e., the H atoms occupy the interstitial sites in the fcc lattice rather than breaking its symmetry. This observation suggests that the planar defects at (111) planes are long-living metastable structures, which eventually will grow into AlH$_3$ [28].

III. DEFECT ENHANCED HYDRIDE FORMATION

Although cracks are usually considered as detrimental defects in material science and engineering, they can be used as a laboratory tool to induce negative pressure, therewith supporting the formation of hydrides without causing complete failure of the material. The stress field of the crack

tip is a function of the stress intensity factor, which itself is proportional to the loading and depends on the geometry of the crack. Thus, it can be envisioned that the loading on the crack provides a continuous variable to probe the negative pressure domain. The interaction of the H excess volume and the long-range stress field of the crack guides the H atoms toward the crack tip regions and induces higher C_H regions near the crack tip, which can serve as hydride nuclei. When the nucleus is formed, it can transform to the most stable hydride. It should be noted that in this regard, the microcracks in the ductile materials have great potential. While the presence of these defects in the material is inevitable, they do not directly lead to failure of it and only make it prone to other failure mechanisms, such as environmentally assisted cracking [36] and stress-corrosion cracking [37].

Microcracks in Al-based alloys are particularly effective in this regard because of the following:

(1) The ductile nature of pure Al combined with alloying, which usually does not show brittle fracture [38], can reduce the damaging effects of hydrides [39,40] by tailoring the interface energies [41]. Alloying and doping are, e.g., used for enhancement of nickel metal hydride batteries [42,43].

(2) The interaction between the excess volume of α-Alane hydride, resulting in a negative strain in the vicinity of the microcrack, and the negative pressure at the crack tip region, stemming from the tensile strain, reduces the formation free energy of this hydride.

Therefore, the excess volume of both individual H atoms and the α-Alane hydride determines the kinetics and thermodynamics of this process. If the excess volume of individual H atoms is low, then the diffusion toward the microcrack will be slow. Moreover, if the excess volume of the desired hydride is low, then the decrease in its formation free energy associated with the presence of the crack stress field, and subsequently the decrease in the required H$_2$ gas pressure, will not be significant.

It is evident from Fig. 6(a) that the external H$_2$ pressure needed for the formation of the hydride at ambient conditions ($p_{tot} = P_{H_2}$ and room temperature) is ≈ 349 MPa, which is larger than the typical practical values of 35–70 MPa [44]. A possible remedy for this problem is including the negative pressure induced by loading cracks.

The spatial dependence of the stress field at the crack tip is

$$p^{(m)}(\vec{r}) = -\frac{1}{3}\sigma_{kk}(\vec{r}) = -\frac{(2+\nu)}{3\sqrt{2\pi}}\frac{K_I}{\sqrt{r}}\cos\frac{\theta}{2}, \qquad (6)$$

where r and θ are the polar coordinates of the point of interest with respect to the crack tip [cf. Fig. 8(a1)], and ν and K_I are the Poisson's ratio and the mode I stress intensity factor, respectively. The cross-sectional area of the cylindrical domain around the crack tip at which the magnitude of the negative pressure is larger than the critical value $p_{crit}^{(m)}$ obtained from Fig. 6(a) will be relevant for hydride formation. Figure 6(b) depicts the dependence of this area, A, on the external hydrogen gas pressure for different stress intensity factors of the crack tip at room temperature. We consider the hydrides with the cross-sectional area of 10π Å^2 as a critical size, as it ensures the presence of second-nearest-neighbor H atoms of an inner H atom in the hydride. The determination of the critical nucleation size of the hydride requires careful calculation of
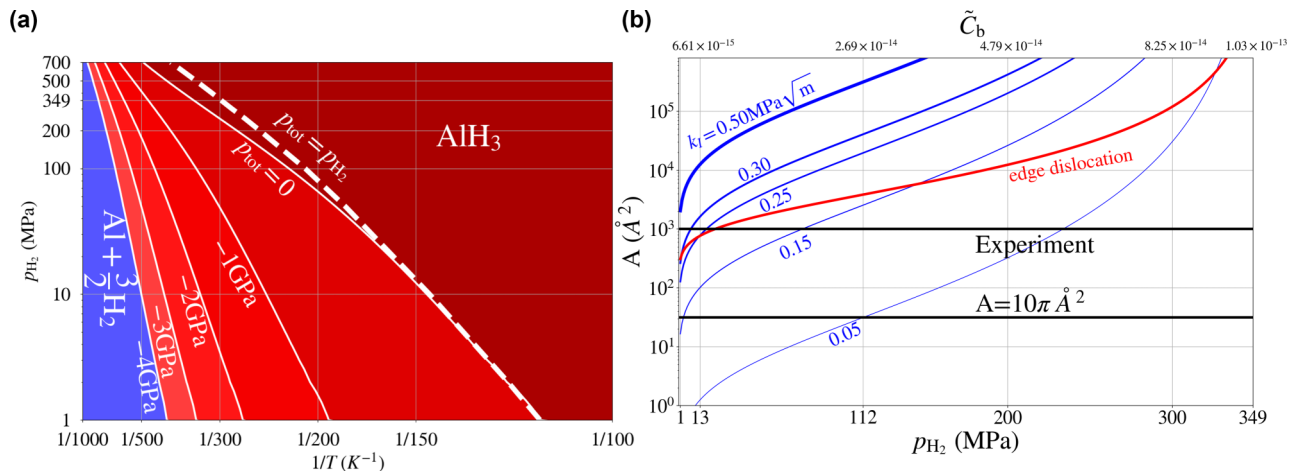
FIG. 6. (a) Pressure-dependent phase diagram of Alane AlH_3 in the $p_{H_2} - T$ space as a function of inverse temperature and external hydrogen pressure (left axis). The plot provides the critical negative mechanical pressure for the formation of the Alane hydride, i.e., $p^{(m)} = p_{tot} - p_{H_2}$. The dashed line denotes the case in which no mechanical load is applied. (b) Dependence of the cross-sectional area, A, around the crack tip for which the conditions allow for hydride formation at $T = 300$ K vs the H_2 pressure for different values of the cracks stress intensity factor k_I. The values of $k_I = 0.3$ MPa$\sqrt{m}$ and $k_I = 0.5$ MPa$\sqrt{m}$ are typical for the emission of dislocations from the crack on a (111) plane and cleavage of the crack on nonemitting crack geometries [38].

the hydride/Al interface energy, which is beyond the scope of this study. The hydrides experimentally observed in this work, which form near the dislocations in crack tip, have a cross-sectional area of ≈ 1000 Å^2.

The presence of a stress intensity factor significantly reduces the external H_2 gas pressure needed for overcoming this critical nucleus size. In the absence of the mechanical loading, i.e., $K_I = 0$, the gas pressure needed for the formation of hydrides is 349 MPa. However, at this pressure, the formation of the hydride is not local and thus the radius of the hydride grows unboundedly. The minimum value of the external pressure required for the formation of *local* hydrides with $A = 10\pi$ Å^2 reduces to ≈ 112 MPa if a K-load of ≈ 0.05 MPa$\sqrt{m}$ is applied. By increasing the stress intensity factor to ≈ 0.15 MPa$\sqrt{m}$, this value decreases to ≈ 2 MPa. For all larger K-loads, with application of 1 MPa of H_2 gas pressure, we can get the minimum-size hydride. In the cases at which the cracks are located along the ductile orientations, the critical load for the emission of dislocations is ≈ 0.30 MPa$\sqrt{m}$ [38]. Since the emission of the dislocations blunts the crack tip, this value is the maximum attainable K-load in the ductile direction. Under this load, the critical H_2 gas pressure is reduced below 1 MPa. A further reduction of the required gas pressure is possible since, in realistic systems, the maximum load can vary between 0.30 MPa$\sqrt{m}$ to loads less than ≈ 0.5 MPa$\sqrt{m}$, which is the cleavage load for the cracks along brittle orientations.

The result shown in Fig. 6(b) indicates that the negative pressure field of the edge dislocation has also an enhancing effect on the hydride formation [22]. However, this effect cannot be tailored by mechanical loading and is not sufficient to form the experimentally observed hydrides.

IV. H ACCUMULATION IN THE CRACK TIP REGION

The fundamental assumption behind the aforementioned analysis is that there exists enough H atoms in the vicinity

of the defect to form the hydride phase and that the system can overcome the energy barrier for hydride formation in pure fcc-Al bulk. Using the example of cracks in Al, we now demonstrate the enhancing effect of the stress field next to microstructural defects on the energetics as well as the formation of *kinetics* of regions with high H concentration at finite temperature. Our MD-MC simulations are concerned with the accumulation of the H atoms at the crack tip region and the formation of any hydride nucleus, not necessarily the Alane hydride. This is due to the high nucleation energy barrier for the formation of Alane hydride, in which Al atoms are no longer in the fcc lattice. Thus capturing this formation with the ADMP requires large timescales. In addition, one requires potentials with DFT accuracy to capture the different bonding states in AlH_2 and AlH_3.

Details of MD-MC simulations

To demonstrate the above-described mechanism, we modified the previously published ADP potential of Al-H to include the first-nearest-neighbor (1NN) and 2NN attractive interaction energies. Based on this potential, MD-MC simulations are performed using the modified scalable parallel Monte Carlo algorithm [45]. The latter explores the phase space in a variance-constrained semi-grand-canonical (VC-SGC) ensemble. Each MC step tries to insert/delete an H atom in/from an empty/filled T site using the Monte Carlo energy criterion as is given in [45]. The ratio of MC attempts to the performed MD steps during the MD-MC simulations is kept as 0.1. The simulations are performed using the large-scale atomic/molecular massively parallel simulator (LAMMPS) [46] and all atomistic figures are created using the OPEN VISUALIZATION TOOL [47].

To examine the enhancement of hydride formation in the defected regions, it is necessary to perform two sets of simulations. In the first set, the samples consist of a defect-free $[l_x \times l_y \times l_z] \approx [316 \times 463 \times 17.1$ Å] box of bulk Al
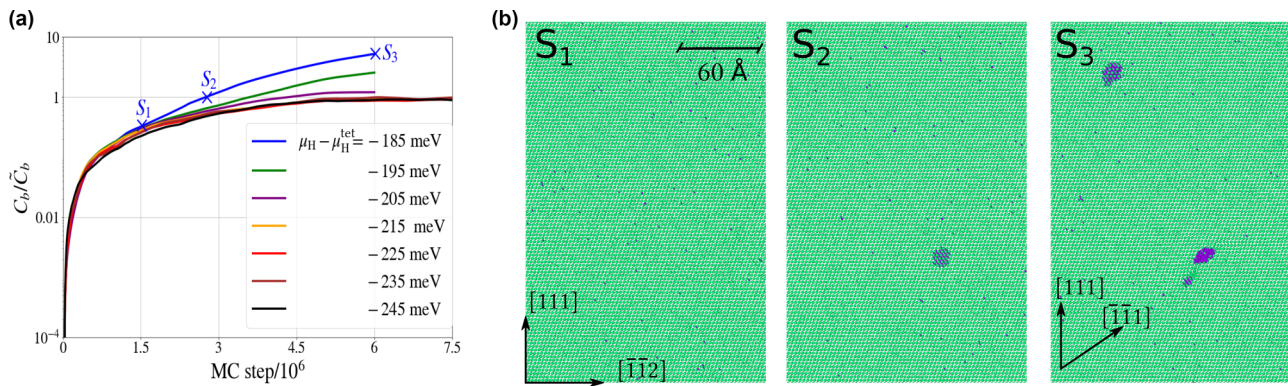
FIG. 7. (a) Evolution of the H concentration vs MC steps in the MD-MC simulations for different chemical potentials of H at $T = 300$ K. The cross symbols indicate the MC steps at which snapshots of atomistic configurations for a subset of a bulk sample with $\mu_H - \mu_H^{tet} = -185$ meV are taken and depicted in (b). The green and purple spheres denote the Al and H atoms, respectively. The snapshots show the nucleation and growth of hydride precipitates.

containing $\approx 153\,000$ Al atoms. The crystallographic vectors of the x, y, and z directions are parallel to $[\bar{1}\bar{1}2]$, $[111]$, and $[\bar{1}10]$, respectively. The samples are equilibrated at 300 K for 50 ps. Afterward, the MD-MC simulations are performed and the concentration of H atoms in the sample is recorded. In these simulations, the chemical potential is kept fixed. The temperature is fixed to room temperature, $T = 300$ K, with a Nosé-Hoover thermostat [48]. The simulations are done in a series of simulation intervals. In each interval, an MD-MC simulation of the semi-grand-canonical ensemble is run for 1 ns, followed by a 20 ps MD run to maintain the temperature and to equilibrate the sample within the canonical ensemble. The time step for the integration in MD simulations is 0.2 fs. The choice of this particularly small integration step ensures a smooth behavior of light H atoms after their addition to the system. Integration steps of less than 0.5 fs were used in the literature in similar studies [49]. The simulation time for the defect-free samples is 15.0 ns and 7.5×10^6 MC steps are performed.

In the second set of simulations, a $(111)[\bar{1}10]$ crack is inserted in the aforementioned sample by omitting the interactions between atoms at the opposite crack faces. The atoms of the sample are displaced according to the asymptotic continuum solution for a semi-infinite mode-I crack in an anisotropic linear elastic crystal [50]. The input parameters for this displacement field are the elastic constants of Al and the mode-I stress intensity factor K_I.

Using the ADMP potential, the elastic constants of Al are computed as $C_{11} = 114$, $C_{12} = 61.6$, and $C_{44} = 31.6$ GPa. K_I is kept less than or equal to 0.30 MPa$\sqrt{m}$, which is the critical load for the emission of dislocations in pure Al. The boundaries of the sample are kept fixed and subsequently the samples are equilibrated at 300 K for 50 ps. After the equilibriation, the above-described MD-MC simulations are performed. Again, the simulations are done in a series of simulation intervals. In each interval, an MD-MC simulation of the grand-canonical ensemble is run for 80 ps and is followed by a 20 ps MD run to maintain the temperature and to equilibrate the sample. The total simulation time is 5 ns and 2.5×10^5 MC steps are performed in each simulation. This number of steps was sufficient to observe the hydride embryos at the crack tip. After performing, the MD-MC simulation, we

relaxed the whole sample using the conjugate gradient method [51] to attain the final structure.

It should be noted that at the first step, we excluded the outermost interstitial sites at the free surfaces of the cracks from the domain of hydride embryo formation. This modification enables us to only focus on the role of the stress field in facilitating hydride embryo formation. This facilitating effect will be generalized to the other types of defects which are not necessarily associated with surfaces. Moreover, we are concerned with the microcracks usually along the grain boundaries inside the material; thus the notion of having a pure Al surface at the crack faces is not reasonable and the faces of the cracks will contain impurities.

Figure 7(a) shows the development of the overall atomic concentration, C_b, of H atoms in Al bulk samples versus the MC attempts in the MD-MC simulations at room temperature. The chemical potential $\mu_H - \mu_H^{tet}$ is kept fixed using a scalable semi-grand-canonical MC algorithm [45]. The concentrations are normalized to the theoretical value of bulk dilute noninteracting H atoms at the given chemical potential, $\tilde{C}_b$. It can be seen that the concentration ratio converges to the constant value of 1 after 10^5 MC steps for $\mu_H - \mu_H^{tet} \leqslant -215$ meV.

For higher chemical potentials, the overall observed concentrations exceed the theoretical prediction as time progresses. This is an indication of a hydride formation in addition to the H in a solid solution. Figure 7(b) illustrates a subset of a crack-free sample with $\mu_H - \mu_H^{tet} = -185$ meV at three different MC steps. It can be seen that regions with high H concentrations form at random locations of the sample with a slight alignment at the $(\bar{1}\bar{1}1)$ plane. These hydride *nuclei* have the structure of fluorite AlH$_2$. The thermodynamic DFT considerations in Sec. II suggest that they will relax to the AlH$_3$ hydride once the hydride becomes large enough to overcome the coherency strain. Capturing the latter mechanism requires more complicated (machine learning) interatomic potentials that can take complex chemical interactions into account. The thermodynamic prediction does not change in the pressure domain $p^{(m)} \leqslant 19.5$ GPa. The reason is that the volume per unit formula of AlH$_2$ is 3.585 Å^3. After the decomposition into $2/3$AlH$_3 + 1/3$Al, it changes to $+8.183$ Å^3. As the corresponding gain in the energy is -0.996 eV
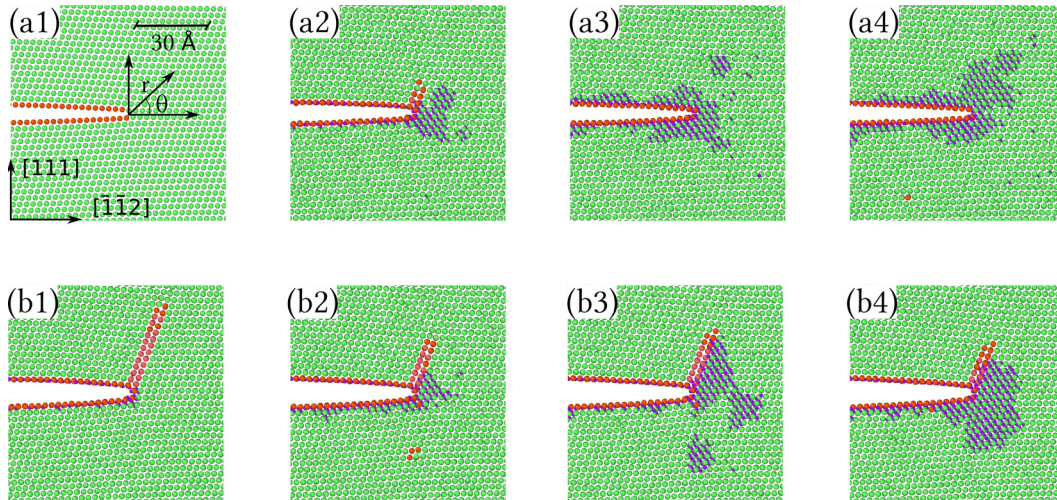
FIG. 8. (a1)–(a4) Atomic structure of the crack tip regions at $T = 300$ K, $K_I = 0.20$ MPa$\sqrt{m}$, and $\mu_H - \mu_H^{tet} = -245, -225, -205, -185$ meV, respectively. (b1)–(b4) Same at $K_I = 0.30$ MPa$\sqrt{m}$. The green, red, and purple spheres denote the fcc-Al, non-fcc Al, and H atoms, respectively.

per Al atom, the lower bound pressure required for inhibiting this transformation by the $p^{(m)}\Delta V$ term is 19.5 GPa, which is far beyond the attainable pressures. Performing the same analysis using the results of the ADMP gives rise to a critical pressure of $p^{(m)} \leqslant 4.5$ GPa. To have a full picture, the large coherency strain of the AlH$_3$ hydride should also be taken into account. To analyze the defected structures, Fig. 8 illustrates the relaxed state of the hydride formed in the crack tip region at $T = 300$ K after 2.5×10^6 of MC steps. It can be seen that the hydride forms at the crack tip at both $K_I = 0.20$ MPa$\sqrt{m}$, 0.30 MPa$\sqrt{m}$ and chemical potentials higher than $\mu_H - \mu_H^{tet} = -225$ meV. Since, for this particular chemical potential, the bulk sample did not form a hydride nucleus after 7.5×10^6 MC steps, one can conclude that the formation of the hydride is enhanced due to the excess volume of H atoms and the stress field of the crack. Therefore, the enhancement of the hydride formation energetics at the crack tip due to its stress field is also accompanied by an increased concentration of the individual H atoms in this particular region and this accumulation enhances the kinetics of hydride formation. More precisely, in the case of the bulk samples, the hydride nucleus at $\mu_H - \mu_H^{tet} = -0.185$ meV forms after 2.65×10^6 MC steps, while in the defected sample with $K_I = 0.3$ MPa$\sqrt{m}$, this nucleus forms at $\mu_H - \mu_H^{tet} = -0.225$ meV and after 2.65×10^6 MC steps.

Interestingly, it can be seen that in all cases with $K_I = 0.30$ MPa$\sqrt{m}$, i.e., close to the previously observed emission loads at 300 K [38], a partial dislocation is emitted. Its emission, in addition to the stacking fault, did not hinder the formation of a hydride nucleus.

For the sake of comparison, we add another simulation in which we do not exclude the free surfaces from the simulations. Figure 9 depicts the key atomistic configuration at the crack tip simulations in this case. It can be seen that the free surfaces are acting as formation nuclei for the hydrides. In this case, we are observing the formation of hydrides at every k-load. In the cases with $\Delta\mu > -205$ meV, we observe that hydrides form at high stressed regions and along the crack faces. This observation demonstrates the enhancing effect of

the free surfaces. If one aims at a complete study of the free surface effects, one should, however, consider that under experimental conditions, an oxide layer often forms at the Al surfaces.

V. EXPERIMENTAL OBSERVATION OF H ENRICHED REGIONS NEAR CRACK TIPS IN A 7449-Al ALLOY

A stress-corrosion cracking, double cantilever beam (DCB) test was performed at room temperature on a commercial 7XXX-aluminium alloy (7449) following the ASTM G168-17 protocol [52]. Precracking was done manually by "pop-in" and droplets of a 3.5% NaCl solution were added twice a day in the slit during weekdays. A series of specimens for atom probe tomography was prepared in the vicinity of the crack tip using a dual beam scanning-electron microscope, Xe-Plasma focused ion beam (FEI Helios PFIB), following the procedure outlined in Ref. [53]. APT data were acquired by a reflectron fitted Local Electrode Atom Probe (LEAP 5000 XR, Cameca Instrument Inc.). We used the voltage-pulsing mode, with a 20% pulse fraction and a pulse repetition rate of 200 kHz. The specimen was maintained at a base temperature of 50 K. The average detection rate was set at 35 ions detected per 10 000 pulses. The data were processed and reconstructed using AP SUITE 6.0, and the tomographic reconstruction was calibrated using the method introduced in Ref. [54]. The scanning electron micrograph (SEM) in Fig. 10 shows the tip of the main crack in the double cantilever beam sample, typically used to study stress-corrosion cracking of Al alloys. The APT sample is prepared within $\approx 1\mu$m from the crack tip. The point cloud obtained from the reconstruction of the APT data is displayed, with blue points corresponding to Al atoms. The green isocomposition surfaces delineate Zn-rich regions (>2 at.%), indicating a large precipitate (η phase) located at a grain boundary along which the crack is propagating. Regions that are rich in hydrogen (>1.6 at.%) are highlighted by a set of red isosurfaces. They form a pattern located in the (111) planes as identified by atom probe crystallography approaches [55,56]. Measuring H by APT is notoriously challenging [57–59], but
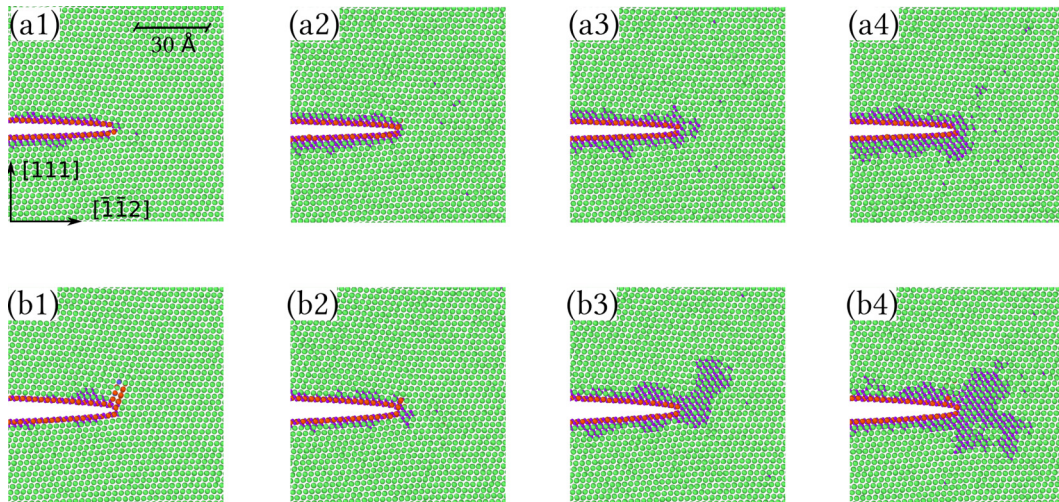
FIG. 9. Same as Fig. 8, but with the surface sites included in the simulations.

we used experimental conditions that minimize the signal from the residual gas in the atom probe chamber. The strong, localized signal can be ascribed to the accumulation of H atoms in the crack tip region along parallel tubular features that were identified by correlative transmission-electron microscopy and APT [56,60,61]. We measure H compositions along a cylindrical region of interest. Here, the H ratio reaches over 6 at.%. Across the multiple acquired datasets, hydrogen ratios of up to 20 at.% and more were recorded at these features, contrasting the concentrations (<1 at.%) measured away from the crack. The distribution of H atoms can be attributed to segregation or to the formation of hydride nuclei at these linear defects.

These results provide experimental evidence that hydrogen tends to be in the stressed regions in the vicinity of the cracks. Here, hydrogen originates from the splitting of water on the freshly formed Al surface exposed by the progression of the crack, i.e., its ingress is likely of a different magnitude as

compared to the cases studied by our atomistic approach. Nevertheless, the theoretical prediction of high equilibrium concentration of H atoms at the crack tip region is still valid.

The observation of a microstructure that appears to be a set of parallel dislocations [56] contained within a (111) plane suggests that hydrogen has a tendency to cause this organization: The presence of the crack and the induced negative pressure attracts H atoms. These H atoms now find the preexisting dislocations at the tip region, accumulate in their local tensile field, and form the hydride. Thus the formation of the high concentration regions is a consequence of the combined effect of crack tip and dislocation stresses. At the same time, the presence of H reduces the distance of piled-up dislocations by a shielding of the repulsive dislocation-dislocation interaction [22]. Moreover, the formation of piled-up dislocations in the crack tip region is connected with stacking faults along the (111) planes, for which the DFT calculations depicted in Fig. 5, and Fig. S1 in the Supplemental Material [21], also
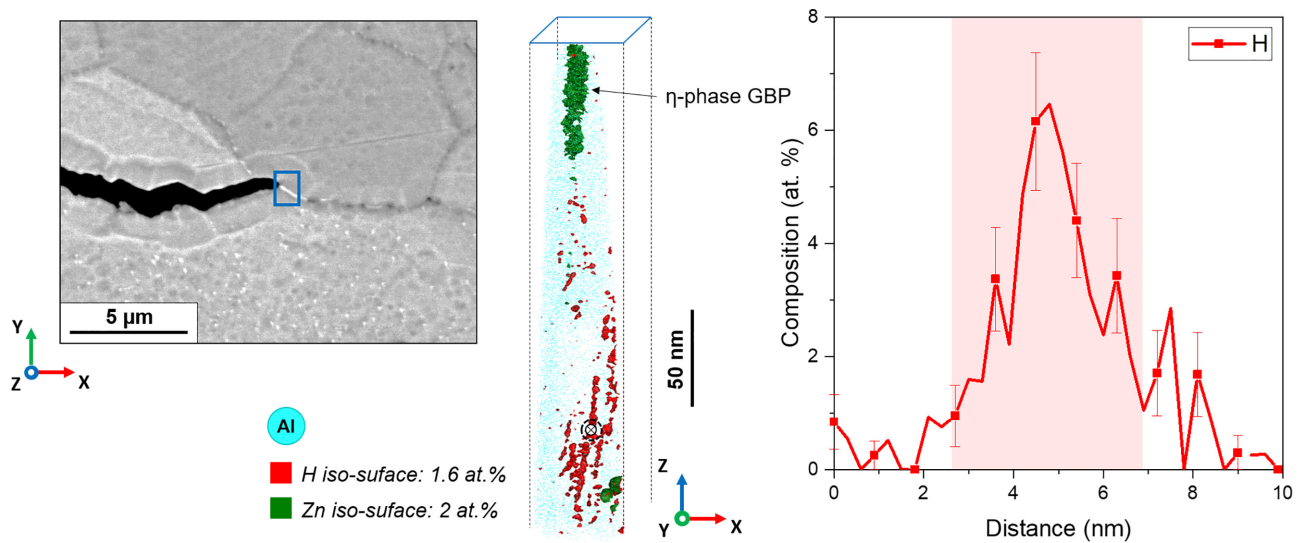

FIG. 10. Left: SEM image depicting the tip of a main crack in a 7449-Al alloy. Middle: APT reconstruction near a stress-corrosion crack tip presenting elongated features on a (111) plane. Right: Composition profile along the *y* axis at the position indicated by the cross in the APT tip.

predict an attraction for H atoms. Out of the planar hydrides, those next to stacking faults even have the lowest formation energy. It should be noted that the segregation of individual H atoms to the generalized stacking faults in Al is considered by Wang *et al.* [62]. They found that the hydrogen concentration at certain sites of the generalized stacking faults of Al can be increased to a few percents at room temperature and $\tilde{C}_b = 1000$ appm. The results of the present work suggest that those hydrogen atoms will form planar hydrides due to complex chemical interactions.

The planar hydrides in the glide plane remain stable even after carving the APT needle out of the sample, which relaxes the crack tip stress, but not the tensile stress of dislocations. Since the formation energy of planar hydrides at the (111) plane is low itself (cf. Fig. S1 in the Supplemental Material [21]), the preference of H atoms to form hydrides along the (111) planes, as discussed in Sec. II, can be understood. It should be noted that the hydrides are not observed at the dislocations far from the crack tip region. The reason is that the negative pressure of single dislocations is too low to thermodynamically stabilize the formation of hydrides with the experimentally observed cross-sectional area at hydrogen pressures lower than 20 MPa [cf. Fig. 6(b)].

VI. SUMMARY AND OUTLOOK

Using *ab initio* and atomistic calculations and supported by experimental results, we have shown that the presence of negatively pressurized regions supports the formation of α-Alane hydride in Al. Using this example, we proved the concept of defects as laboratory tools for exploring constrained equilibria [63,64], in this case the negative pressure domain, of a phase diagram. In particular, the unique property of cracks to continuously and measurably change the negative pressure in the material when the applied loads are modified provides an opportunity to systematically investigate the properties of hydrides. Cracks also show a unique potential for facilitating the charging and discharging process of metal hydrides. These investigations are crucial for tackling major technological problems arising against using hydrogen as a energy carrier.

Herewith, we propose a route for tailoring negative pressure through defects, which can be considered as a remedy for enhancing metal hydride formation. The information about the critical stress intensity factors for emission of dislocations and decohesion in Al can be used for the determination of a safe magnitude of external applied load by which the hydrides form prior to the propagation or blunting of cracks. The presence of suitable alloying elements can ensure the presence of initial cracks with a suitable length in metals. The criteria for choosing the solutes are twofold: (1) While they should destabilize the interfaces without hydrogen, their contribution to hydrogen embrittlement must be limited, and (2) their presence in bulk should enhance the negative pressure-dependent solubility of hydrogen in the matrix. Therefore, finding suitable solutes requires systematic investigations beyond the current state of the art in the literature [65–67]. This enhancing effect has certain implications for H-storage applications.

The interaction of hydrogen next to cracks and dislocations is also decisive for the study of hydrogen embrittlement. For example, previous theoretical studies suggest that nanohydrides can induce ductile-to-brittle transitions [49,68] in nickel. On the other hand, the presence of hydrides can facilitate the nucleation of dislocations [69] and probably make the material more locally ductile [70]. Thus, using cracks as a tool for investigating the behavior of hydrides opens a different horizon for scientific and technologically relevant research.

[1] V. Smil, *Energy and Civilization: A History* (MIT Press, Cambridge, MA, 2018).

[2] J. G. J. Olivier, K. M. Schure, J. A. H. W. Peters *et al.*, PBL Netherlands Environmental Assessment Agency **5**, 1 (2017).

[3] F. Dawood, M. Anda, and G. Shafiullah, Intl. J. Hydrogen Energy **45**, 3847 (2020).

[4] L. Klebanoff and J. Keller, Sandia National Laboratories, Report No. SAND2012-0786 (Sandia National Laboratories, Albuquerque, NM, 2012).

[5] D. B. Smith, R. C. Bowman, L. M. Anovitz, C. Corgnale, and M. Sulic, J. Phys. Energy **3**, 034004 (2021).

[6] A. R. Imre, Phys. Status Solidi B **244**, 893 (2007).

[7] P. F. Mcmillan, High Press. Res. **23**, 7 (2003).

[8] P. F. McMillan, Nat. Mater. **1**, 19 (2002).

[9] S. Siol, A. Holder, J. Steffes, L. T. Schelhas, K. H. Stone, L. Garten, J. D. Perkins, P. A. Parilla, M. F. Toney, B. D. Huey *et al.*, Sci. Adv. **4**, eaaq1442 (2018).

[10] A. Gupta, B. Tas, D. Korbmacher, B. Dutta, Y. Neitzel, B. Grabowski, T. Hickel, V. Esin, S. V. Divinski, G. Wilde *et al.*, Materials **14**, 1837 (2021).

[11] W. Jiang, H. Wang, and M. Zhu, Rare Metals **40**, 3337 (2021).

[12] J. Graetz and B. C. Hauback, MRS Bull. **38**, 473 (2013).

[13] J. Graetz, J. Reilly, V. Yartys, J. Maehlen, B. Bulychev, V. Antonov, B. Tarasov, and I. Gabis, J. Alloys Compd. **509**, S517 (2011).

[14] G. Kresse and J. Hafner, Phys. Rev. B **47**, 558 (1993).

[15] G. Kresse and J. Furthmüller, Comput. Mater. Sci. **6**, 15 (1996).

[16] G. Kresse and J. Furthmüller, Phys. Rev. B **54**, 11169 (1996).

[17] J. P. Perdew, K. Burke, and M. Ernzerhof, Phys. Rev. Lett. **77**, 3865 (1996).

[18] M. Methfessel and A. T. Paxton, Phys. Rev. B **40**, 3616 (1989).

[19] C. Freysoldt, B. Grabowski, T. Hickel, J. Neugebauer, G. Kresse, A. Janotti, and C. G. Van de Walle, Rev. Mod. Phys. **86**, 253 (2014).

[20] C. Wolverton, V. Ozoliņš, and M. Asta, Phys. Rev. B **69**, 144109 (2004).

[21] See Supplemental Material at http://link.aps.org/supplemental/10.1103/PhysRevMaterials.7.105401 for more details.

[22] J. von Pezold, L. Lymperakis, and J. Neugebauer, Acta Mater. **59**, 2969 (2011).

[23] H. Birnbaum, C. Buckley, F. Zeides, E. Sirois, P. Rozenak, S. Spooner, and J. Lin, J. Alloys Compd. **253-254**, 260 (1997).

[24] F. Apostol and Y. Mishin, Phys. Rev. B **82**, 144115 (2010).

[25] D. Xie, S. Li, M. Li, Z. Wang, P. Gumbsch, J. Sun, E. Ma, J. Li, and Z. Shan, Nat. Commun. **7**, 13341 (2016).

[26] D.-G. Xie, L. Wan, and Z.-W. Shan, Corrosion Sci. **183**, 109307 (2021).

[27] A. Tehranchi, B. Yin, and W. Curtin, Philos. Mag. **97**, 400 (2017).

[28] A. Tehranchi, S. Zhang, A. Zendegani, C. Scheu, T. Hickel, and J. Neugebauer, arXiv:2303.07504.

[29] Y. Fukai, *The Metal-hydrogen System: Basic Bulk Properties*, Vol. 21 (Springer Science & Business Media, Berlin-Heidelberg, 2005).

[30] G. C. Sih, P. Paris, and G. Irwin, Intl. J. Fract. Mech. **1**, 189 (1965).

[31] V. Yamakov, E. Saether, D. R. Phillips, and E. H. Glaessgen, J. Mech. Phys. Solids **54**, 1899 (2006).

[32] A. Van der Ven and G. Ceder, Acta Mater. **52**, 1223 (2004).

[33] B. Grabowski, T. Hickel, and J. Neugebauer, Phys. Rev. B **76**, 024309 (2007).

[34] P. W. Atkins and J. De Paula, *Physical Chemistry* (Oxford University Press, Oxford, UK, 1998).

[35] C. San Marchi, B. P. Somerday, and S. L. Robinson, Intl. J. Hydrogen Energy **32**, 100 (2007).

[36] R. Braun, Materialwiss. Werkstofftech. **38**, 674 (2007).

[37] A. U. Rao, V. Vasu, M. Govindaraju, and K. S. Srinadh, Transact. Nonferrous Metals Soc. China **26**, 1447 (2016).

[38] V. Yamakov, D. Warner, R. Zamora, E. Saether, W. Curtin, and E. Glaessgen, J. Mech. Phys. Solids **65**, 35 (2014).

[39] S. Ciaraldi, J. Nelson, R. Yeske, and E. Pugh, Studies of hydrogen embrittlement and stress-corrosion cracking in an aluminum-zinc-magnesium alloy [5.6 Zn-2.6Mg], Tech. Rep. No. DOE/ER/01198-1325 (Illinois University, Dept. of Metallurgy and Mining Engineering, Urbana, IL, 1980).

[40] J. Scully, G. Young, Jr., and S. Smith, in *Gaseous Hydrogen Embrittlement of Materials in Energy Technologies*, edited by R. P. Gangloff and B. P. Somerday (Woodhead Publishing, Cambridge UK, 2012), pp. 707–768.

[41] D.-l. Zhang, W. Jiong, K. Yi, Z. You, and D. Yong, Transact. Nonferrous Metals Soc. China **31**, 3342 (2021).

[42] M. Tsukahara, K. Takahashi, A. Isomura, and T. Sakai, J. Alloys Compd. **287**, 215 (1999).

[43] M. Tsukahara, K. Takahashi, T. Mishima, A. Isomura, and T. Sakai, J. Alloys Compd. **253-254**, 583 (1997).

[44] M. Monde, P. Woodfield, T. Takano, and M. Kosaka, Intl. J. Hydrogen Energy **37**, 5723 (2012).

[45] B. Sadigh, P. Erhart, A. Stukowski, A. Caro, E. Martinez, and L. Zepeda-Ruiz, Phys. Rev. B **85**, 184203 (2012).

[46] S. Plimpton, J. Comput. Phys. **117**, 1 (1995).

[47] A. E. Stukowski, Model. Simul. Mater. Sci. Eng. **18**, 015012 (2010).

[48] S. Nosé, J. Chem. Phys. **81**, 511 (1984).

[49] J. Song and W. Curtin, Nat. Mater. **12**, 145 (2013).

[50] Z. Wu and W. A. Curtin, Acta Mater. **88**, 1 (2015).

[51] M. Hestenes and E. Stiefel, J. Res. Natl. Bur. Stand. **49**, 409 (1952).

[52] *ASTM G168-17: Standard Practice for Making and Using Precracked Double Beam Stress Corrosion Specimens* (ASTM International, West Conshohocken, PA, 2017).

[53] B. Gault, A. J. Breen, Y. Chang, J. He, E. A. Jägle, P. Kontis, P. Kürnsteiner, A. K. da Silva, S. K. Makineni, I. Mouton *et al.*, J. Mater. Res. **33**, 4018 (2018).

[54] B. Gault, M. P. Moody, F. De Geuser, G. Tsafnat, A. La Fontaine, L. T. Stephenson, D. Haley, and S. P. Ringer, J. Appl. Phys. **105**, 034913 (2009).

[55] B. Gault, M. P. Moody, J. M. Cairney, and S. P. Ringer, Mater. Today **15**, 378 (2012).

[56] X. Zhou, J. R. Mianroodi, A. Kwiatkowski da Silva, T. Koenig, G. B. Thompson, P. Shanthraj, D. Ponge, B. Gault, B. Svendsen, and D. Raabe, Sci. Adv. **7**, eabf0563 (2021).

[57] M. S. Meier, M. E. Jones, P. J. Felfer, M. P. Moody, and D. Haley, Microsc. Microanal. **28**, 1231 (2022).

[58] G. Sundell, M. Thuvander, and H.-O. Andrén, Ultramicroscopy **132**, 285 (2013).

[59] A. J. Breen, L. T. Stephenson, B. Sun, Y. Li, O. Kasian, D. Raabe, M. Herbig, and B. Gault, Acta Mater. **188**, 108 (2020).

[60] M. Kuzmina, M. Herbig, D. Ponge, S. Sandlöbes, and D. Raabe, Science **349**, 1080 (2015).

[61] S. K. Makineni, A. Kumar, M. Lenz, P. Kontis, T. Meiners, C. Zenk, S. Zaefferer, G. Eggeler, S. Neumeier, E. Spiecker *et al.*, Acta Mater. **155**, 362 (2018).

[62] Y. Wang, D. Connétable, and D. Tanguy, Philos. Mag. **99**, 1184 (2019).

[63] Y. B. Kang, Calphad **50**, 23 (2015).

[64] P. Koukkari and R. Pajarre, Calphad **30**, 18 (2006).

[65] S. Wu, H. S. Soreide, B. Chen, J. Bian, C. Yang, C. Li, P. Zhang, P. Cheng, J. Zhang, Y. Peng, G. Liu, Y. Li, H. J. Roven, and J. Sun, Nat. Commun. **13**, 3495 (2022).

[66] M. López Freixes, X. Zhou, H. Zhao, H. Godin, L. Peguet, T. Warner, and B. Gault, Nat. Commun. **13**, 4290 (2022).

[67] J. Hu, Z. Xiao, and Y. Huang, Mater. Sci. Eng. A **800**, 140261 (2021).

[68] J. Song and W. A. Curtin, Acta Mater. **59**, 1557 (2011).

[69] G. Leyson, B. Grabowski, and J. Neugebauer, Acta Mater. **107**, 144 (2016).

[70] H. K. Birnbaum and P. Sofronis, Mater. Sci. Eng., A **176**, 191 (1994).